Supplement to Spatiotemporal Dynamics of Clusters in the Bridge Zone Linking L'Aquila 2009 and Central Italy 2016 Seismic Sequences

Alessandro Vuan ⓘ * [1,2], **Lauro Chiaraluce** ⓘ [2,1], **Saeed Yahya Mohanna** ⓘ [3], **Monica Sugan** ⓘ [1]

[1]Department of Seismological Research, National Institute of Oceanography and Applied Geophysics - OGS, Trieste, Italy,

[2]National Earthquake Observatory, National Institute of Geophysics and Volcanology - INGV, Rome, Italy, [3]Department of

Earth, Planetary, and Sciences, University of California Los Angeles - Los Angeles, CA, USA

The Supplement includes some sections providing additional information on clustering, key formulas to calculate the fault strength decrease by using diffusivity value, three Movies to support seismicity patterns and visualize the clusters' orientations, and eight additional Figures providing support to the main text.

1   Clustering Method

Among the various methods recently employed in seismology for the spatio-temporal clustering of seismic events, the literature includes DBSCAN (Ester et al., 1996) and HDBSCAN (Campello et al., 2013, 2015). DBSCAN and HDBSCAN have different clustering approaches, parameter sensitivity, handling of cluster shape and noise, and output management. Regarding the different approaches to the problem, DBSCAN operates a flat clustering and finds clusters simply based on density, labelling points as core, border or noise while HDBSCAN builds a hierarchy of clusters and extracts the most stable ones.

In HDBSCAN, the number of critical input parameters is reduced and robustness improved by removing the need for the radius parameter. The DBSCAN algorithm has certain shortcomings, one of which is that it cannot determine two fundamental parameters (the neighborhood of a point and the minimum number of points) by itself, and the other is that it takes a long time to traverse all points when the dataset is large (Ma et al., 2023). The radius parameter in DBSCAN defines the maximum distance between two points for them to be considered neighbors. It is a crucial parameter for determining the density of a neighborhood and is used to classify points as core, border, or noise points. Choosing an appropriate radius is critical, as a value that is too small can classify too many points as noise, while a value that is too large can merge distinct clusters. The comparison between DBSCAN

---

*Corresponding author: avuan@ogs.it

and HDBSCAN reveals strengths and limitations and the choice between them depends critically on the specific application requirements and data characteristics.

DBSCAN and modified versions of it can offer advantages such as specificity and precision. This makes DBSCAN particularly suitable for limited blind searches and scenarios where falsely identifying non-existent clusters would be more problematic than missing some true clusters (de Berg et al., 2017). HDBSCAN's superior sensitivity of up to 82% compared to DBSCAN's 50–62% (Hunt and Reffert, 2021) makes it the stronger choice. Its ability to handle varying density environments and detect clusters across all density ranges particularly benefits analyses of heterogeneous datasets as in our case. We also preferred HDBSCAN because its parameter setup was described as easier and more intuitive, though careful parameter selection remained necessary to balance sensitivity against false positive rates (Hunt and Reffert, 2021).

Using silhouette score for tuning makes HDBSCAN more automated but adds complexity: instead of one parameter (minimum cluster size), a range and an evaluation metric has to be managed. We used the silhouette score to find the optimal number of clusters (higher silhouette score usually indicates better clustering). The Silhouette Coefficient is calculated using the mean intra-cluster distance (a) and the mean nearest-cluster distance (b) for each sample. It is defined as:

$$s = \frac{b - a}{\max(a, b)} \tag{1}$$

where:

- a is the average distance between a sample and all other points in the same cluster (intra-cluster distance).

- b is the average distance between a sample and the points in the nearest cluster that the sample is not a part of.

Note that the Silhouette Coefficient is only defined if the number of labels satisfies:

$$2 \leq n_{\text{labels}} \leq n_{\text{samples}} - 1 \tag{2}$$

In the Figure S4, we show the minimum cluster size versus the silhouette score for the time windows specified in Table 1. For finding the optimum number of clusters, we iterate the calculation of the silhouette score from 40 to 800 events with a step of 20.

2 Pore Fluid Pressure Diffusion Formulas

This subsection outlines the method proposed by Malagnini et al. (2010, 2012) to estimate the reduction in fault strength following a mainshock. The approach combines pore fluid pressure diffusion with

60 fault mechanical parameters to quantify how elevated fluid pressures progressively weaken the fault
61 zone, promoting slip and cluster migration. The key components are described in Table S1.

Table S1 Model variables and their units

Symbol	Description	Units
P_f	Pore fluid pressure	Pa
P_0	Pressure at origin	Pa
P_1	Initial pressure away from origin	Pa
D	Hydraulic diffusivity	m^2/s
x	Distance from origin	m
t	Time since mainshock	s
z	Depth	m
λ_f	Pore fluid pressure coefficient	–
ρ_r	Rock density	kg/m^3
ρ_w	Fluid density	kg/m^3
g	Acceleration due to gravity	m/s^2
θ	Angle between fault and σ_1	rad
μ_s	Static friction coefficient	–
σ_n	Normal stress on fault	Pa
τ_y	Shear stress (fault strength)	Pa
z_{gt}	Gradient transition depth	m

62 For a distance x from the origin and time t, the pore fluid pressure $P_f(x,t)$ is given by:

$$P_f(x,t) = \begin{cases} (P_0 - P_1)\ \text{erfc}\left(\dfrac{x}{2\sqrt{Dt}}\right) + P_1, & \text{steady-state,} \\[2mm] \dfrac{(P_0 - P_1)}{2}\ \text{erfc}\left(\dfrac{x}{2\sqrt{Dt}}\right) + P_1, & \text{non-steady-state,} \end{cases} \tag{3}$$

64 where:

$$P_0 = \lambda_f \rho_r g z, \qquad P_1 = \rho_w g z, \tag{4}$$

66 in which erfc(y) = 1-erf(y) is the complementary error function, erf(y) is the error function, and D is the
67 hydraulic diffusivity.

2.1 Gradient Transition Depth

69 This subsection quantifies the depth at which the pressure gradient changes significantly, marking the
70 transition between fluid-dominated and lithostatic regimes. The formula links pore pressure to rock
71 density and depth, providing insight into how fluid pressure modifies effective stress conditions. Below,
72 λ expresses the ratio of pore pressure to lithostatic pressure, and z_{gt} estimates the depth where this ratio
73 alters stress balance.

$$\lambda = \frac{P_f}{\rho_r g z}, \qquad z_{gt} = \frac{\rho_r z (1 - \lambda)}{\rho_r - \rho_w}. \tag{5}$$

3

2.2 Fault Stress Components

This subsection calculates the normal stress acting on faults of different types (normal, thrust, strike-slip) as a function of depth, fault orientation, and density contrast. These stresses are critical for evaluating fault strength reduction under elevated pore pressure. Finally, shear stress (fault strength) expresses how frictional resistance scales with normal stress, which is reduced when pore pressure increases.

Normal fault:

$$\sigma_n = \frac{g\,z\,(\rho_r - \rho_w)\sin\theta}{\mu_s \cos\theta + \sin\theta}. \tag{6}$$

Thrust fault:

$$\sigma_n = \frac{g\,z\,(\rho_r - \rho_w)\cos\theta}{\cos\theta - \mu_s \sin\theta}. \tag{7}$$

Strike-slip fault:

$$\sigma_n = \frac{g\,z\,(\rho_r - \rho_w)\sin(2\theta)}{\mu_s \cos(2\theta) + \sin(2\theta)}. \tag{8}$$

The shear stress (fault strength) is:

$$\tau_y = \mu_s \sigma_n. \tag{9}$$

3 Movies

Movies are uploaded as external mp4 files. M1 and M2 illustrate the evolution of seismicity in the CSZ following the two mainshocks in 2009 and 2016, respectively. Movie M3 provides insight into the orientation of seismic clusters along the defined planes.

Movie M1 – Temporal evolution of seismicity in the Campotosto Seismic Zone (CSZ) following the 2009 L'Aquila Earthquake (M_W 6.3, April 6, 2009). The animation consists of two synchronized panels: Top Panel: Map view displaying the spatial distribution of seismic events across the CSZ. Bottom Panel: Longitude–Depth cross-section illustrating the vertical distribution of events along the east-west axis. Seismic events are represented as colored dots, with color encoding the time of occurrence relative to the mainshock, enabling visualization of the temporal migration of seismicity.

Movie M2 – Temporal evolution of seismicity in the Campotosto Seismic Zone (CSZ) following the 2016 Amatrice Earthquake (M_W 6.1, August 24, 2016). The animation consists of two synchronized panels: Top Panel: Map view displaying the spatial distribution of seismic events across the CSZ. Bottom Panel: Longitude–Depth cross-section illustrating the vertical distribution of events along the east-west axis. Seismic events are represented as colored dots, with color encoding the time of occurrence relative to the mainshock, enabling visualization of the temporal migration of seismicity.

Movie M3 – Horizontal rotation in the seismogenic volume containing clustered events. The animation presents a horizontal rotation of the 3D volume encompassing seismic clusters, which are geometrically approximated by planar surfaces as shown in Figure 6. The rotation provides a dynamic perspective on the spatial relationships and orientations of the clusters, enhancing the visualization of their structural configuration within the crust.

4   Figures

Figure S1 presents the frequency–magnitude distribution of events from the three high-resolution catalogs used. Figure S2 highlights variations in strike angles derived from focal mechanism solutions. Figure S3 shows changes in seismicity rates in the CSZ, both south and north of the mainshock areas. Figure S4 displays the silhouette score versus the number of clusters. Figure S5 is about unclustered seismicity within selected time windows. Figure S6 represents an example of PCA analysis to determine the best orientation of the cluster's plane. Figure S7 reveals short-term variations in the migration behavior of small clusters during the period (2010–2016). Figure S8 reports seismic front diffusivity for clusters in Figure S7.
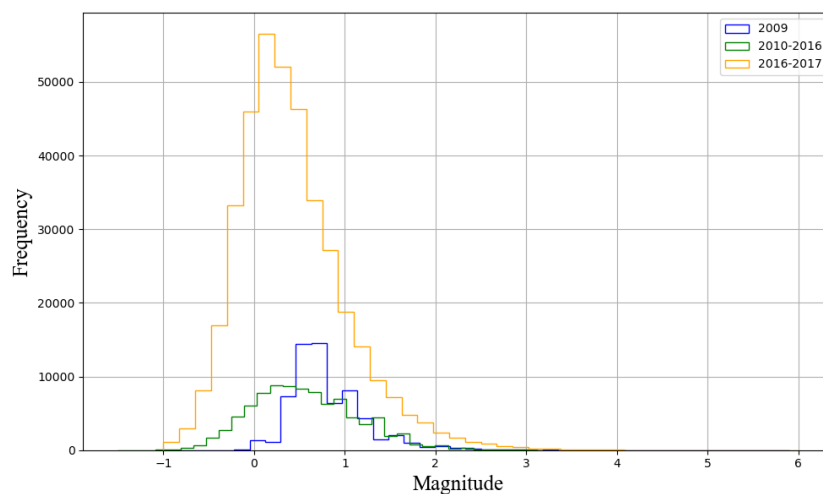

Figure S1   Magnitude–Frequency distributions from high-resolution seismic catalogs. This figure compares the magnitude–frequency distributions derived from three distinct high-resolution earthquake catalogs: (Valoroso et al., 2013; Sugan et al., 2023; Waldhauser et al., 2021). The distributions highlight similarities and differences in completeness magnitude and event density across the datasets, reflecting variations in temporal coverage, detection thresholds, and cataloging methodologies.
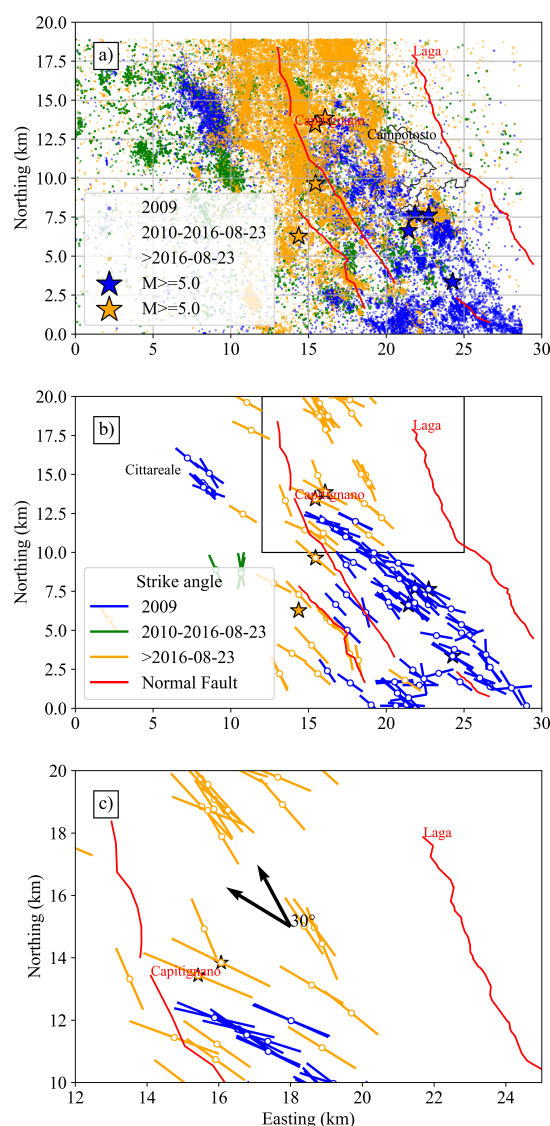
Figure S2 Seismicity and focal mechanism analysis in the CSZ (2009–2017) (a). Map view of seismicity in the Campotosto area during the 2009–2017 time window. Colored dots correspond to earthquake events from the three high-resolution catalogs listed in Table 1. (b) Strike angles of focal mechanisms for events with magnitude M > 3, compiled from Brennan Brunsvik et al. (2021); Locchi et al. (2024). (c) Zoomed-in view of panel (b), emphasizing the rotation in strike angles observed in the northwestern sector. Red lines indicate the surface trace of major SW-dipping normal faults, as mapped by Faure Walker et al. (2021), and serve as structural references.
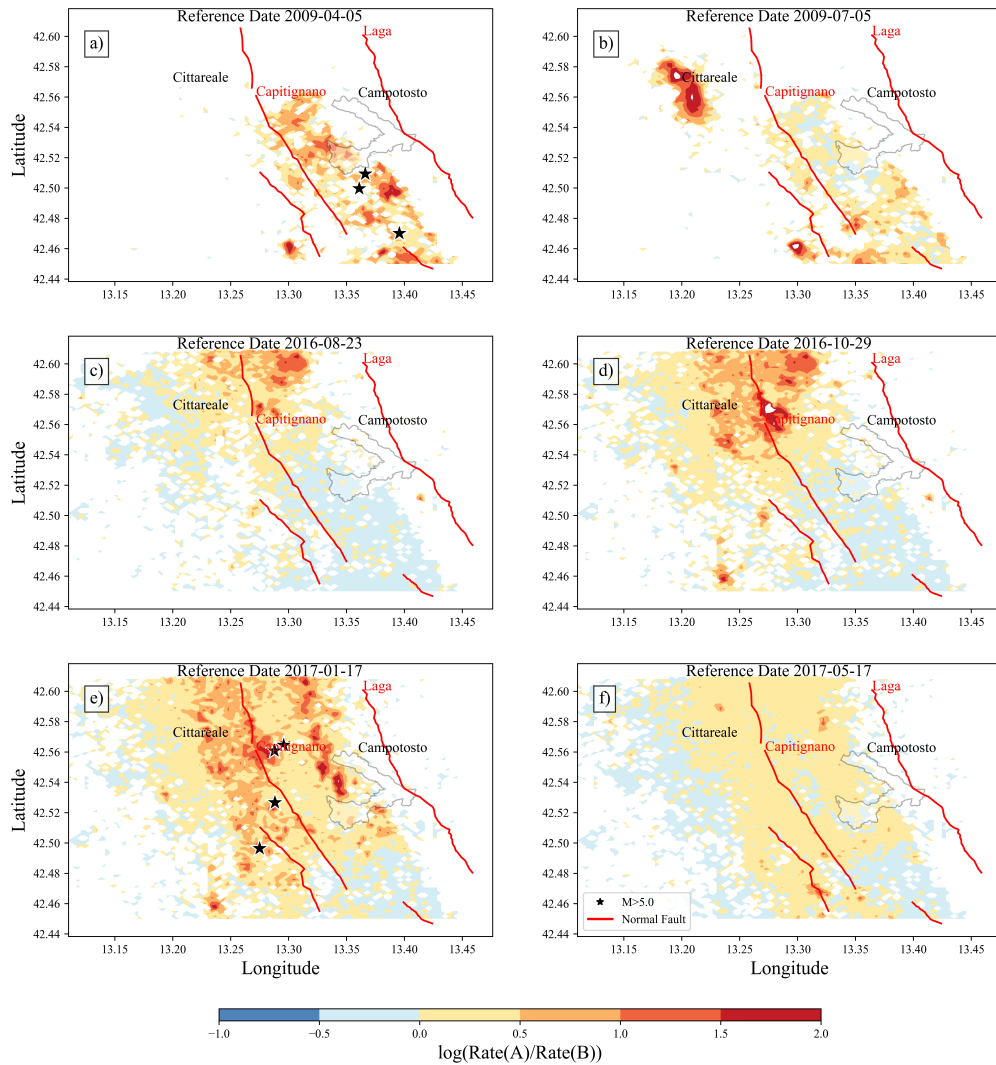
Figure S3 Seismicity rate variations in the Campotosto Seismic Zone (CSZ) across key changing point dates (0–20 km Depth Range). Seismicity rate changes are computed on a 0.3 km grid as the logarithmic ratio of event counts in two 2.5-month windows: before (B) and after (A) each reference date. Six reference dates were selected to capture major seismic transitions associated with: (a) the M_w 6.3 L'Aquila mainshock, (b) the Cittareale seismic sequence, (c) the M_w 6.1 Amatrice mainshocks, (d) the M_w 6.5 Norcia mainshock, (e) the activation of four M_w > 5 events within a single day, and (f) the subsequent seismic quiescence in 2017. Black stars mark events with M_w > 5.0. Red lines indicate the surface trace of SW-dipping normal faults (Faure Walker et al., 2021). The outline of the Campotosto water reservoir is also shown for spatial reference.
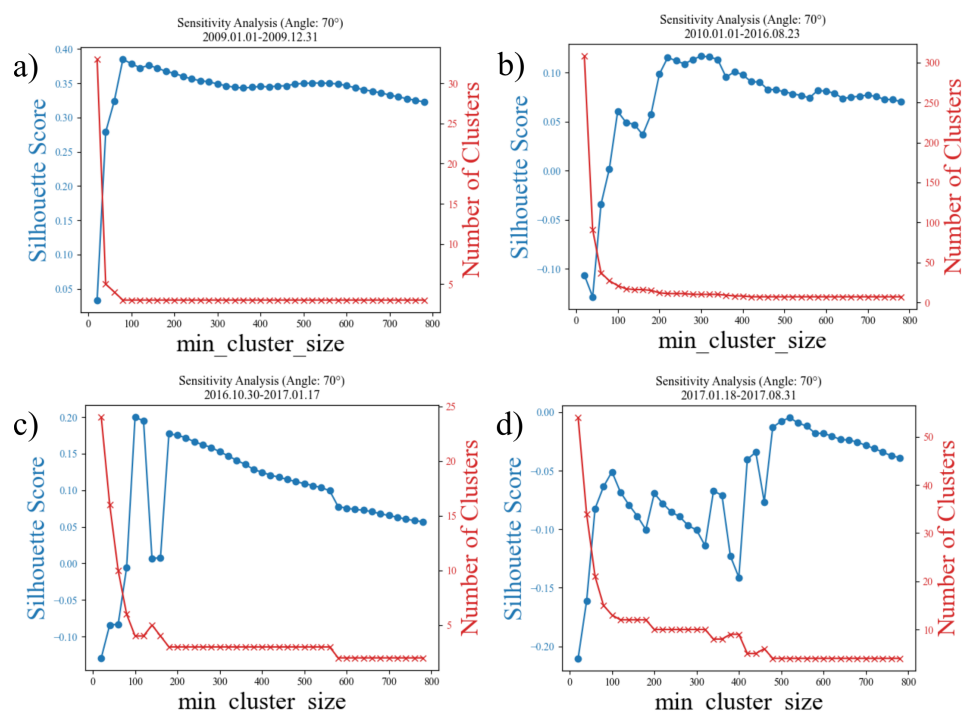
Figure S4 Minimum cluster size versus silhouette score and number of clusters for the time windows specified in Table 1.
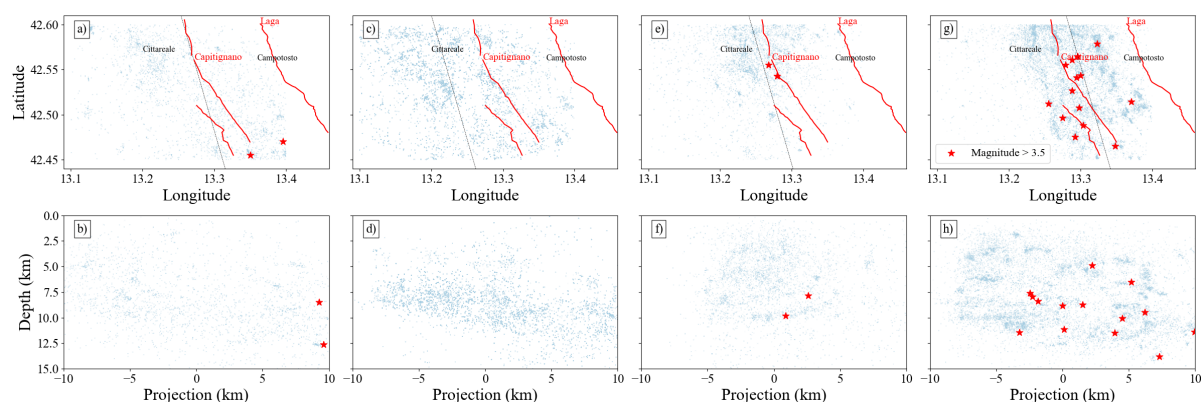

Figure S5 Residual seismicity retained after HDBSCAN cluster extraction. This figure displays the residual background seismicity in the CSZ following the removal of clustered events using the HDBSCAN algorithm. The analysis spans the same time intervals as those presented in Figure 4. The remaining events represent diffuse seismicity not associated with high-density clusters, offering insight into the spatial and temporal distribution of background activity.
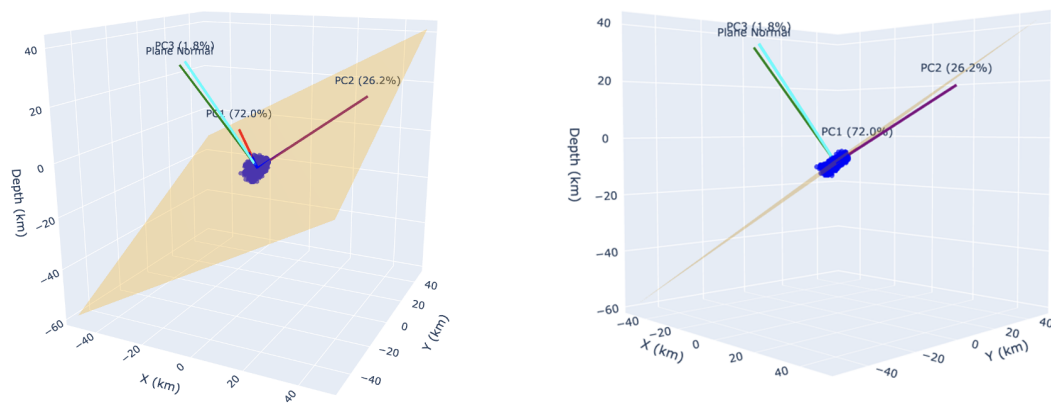
Figure S6   PCA analysis for cluster A1 to determine the plane orientation. The variance distribution along the two principal in-plane directions: approximately 72% of events align with PC1 and 28% with PC2. The third component (PC3), representing the out-of-plane direction, exhibits minimal variance.

Cluster	PC1 (%)	PC2 (%)	PC3 (%)	PC1_angle (°)
A0	50.70	36.20	13.10	99.62
A1	71.99	26.21	1.81	-35.54
A2	71.68	17.85	10.47	-33.51
C0	77.45	20.43	2.12	7.47
C1	63.39	29.81	6.80	-3.80
C2	68.21	27.28	4.51	-144.04
C3	69.25	23.67	7.08	132.66
C4	45.62	35.82	18.56	-15.45
C5	45.16	36.36	18.49	65.77
C6	65.08	29.67	5.24	-17.14
C7	59.26	28.84	11.90	132.52
C8	63.90	18.88	17.21	-63.25
C9	79.99	13.83	6.19	-22.00
E0	79.18	14.92	5.90	-5.61
E1	55.89	39.04	5.08	7.37
E2	71.32	23.56	5.12	1.65
E3	58.21	34.23	7.56	23.37
G0	68.23	17.28	14.48	10.08
G1	89.11	8.91	1.98	-20.94
G2	89.45	8.16	2.39	-21.53
G3	59.31	31.24	9.45	65.00

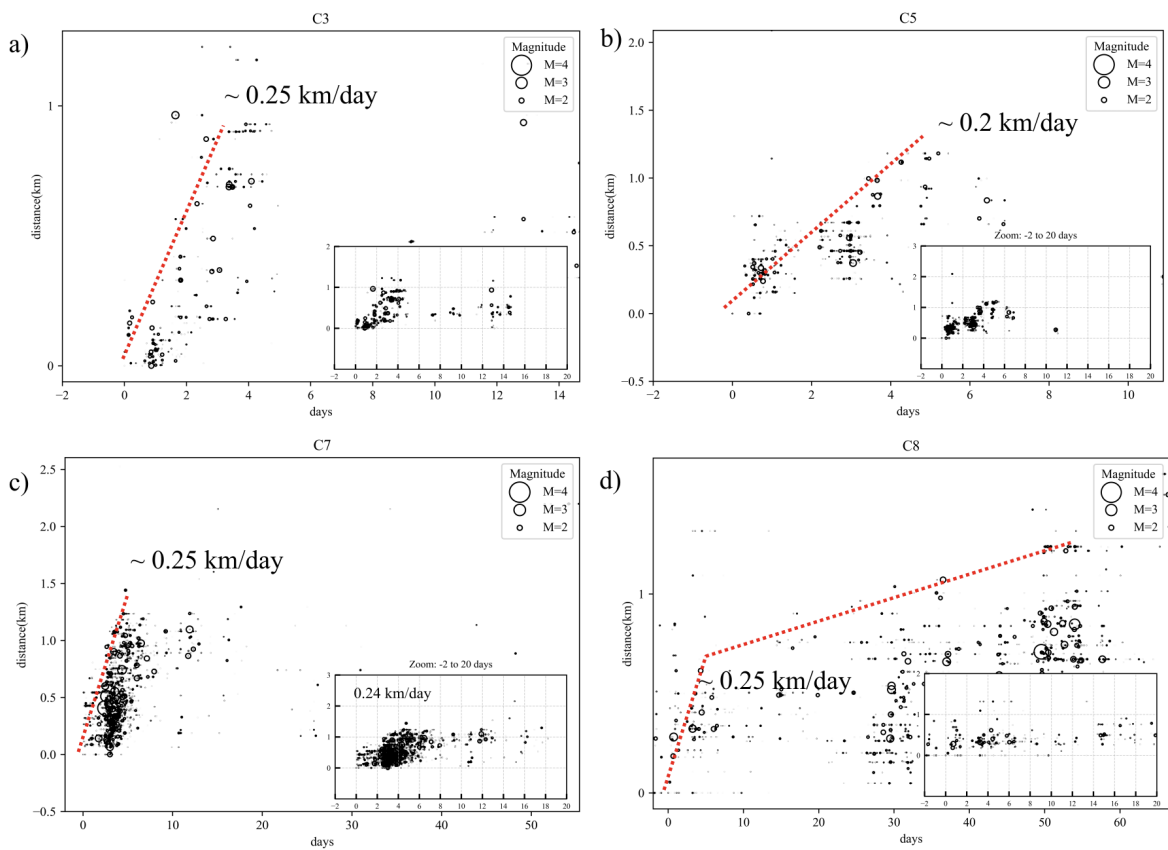**Table S2** Principal component percentages and PC1 orientation angle relative to North for each cluster.

Figure S7 Seismicity front migration for clusters C3, C5, C7, and C8. Panels (a)–(d) illustrate the temporal evolution of the seismicity front for clusters C3, C5, C7, and C8, respectively. The red dotted lines represent the 90th percentile of the 3D radial distance from the initial event in each cluster, serving as a proxy for the migration velocity of seismic activity. Insets provide zoomed-in views of selected time intervals to highlight short-term fluctuations and variations in migration dynamics.
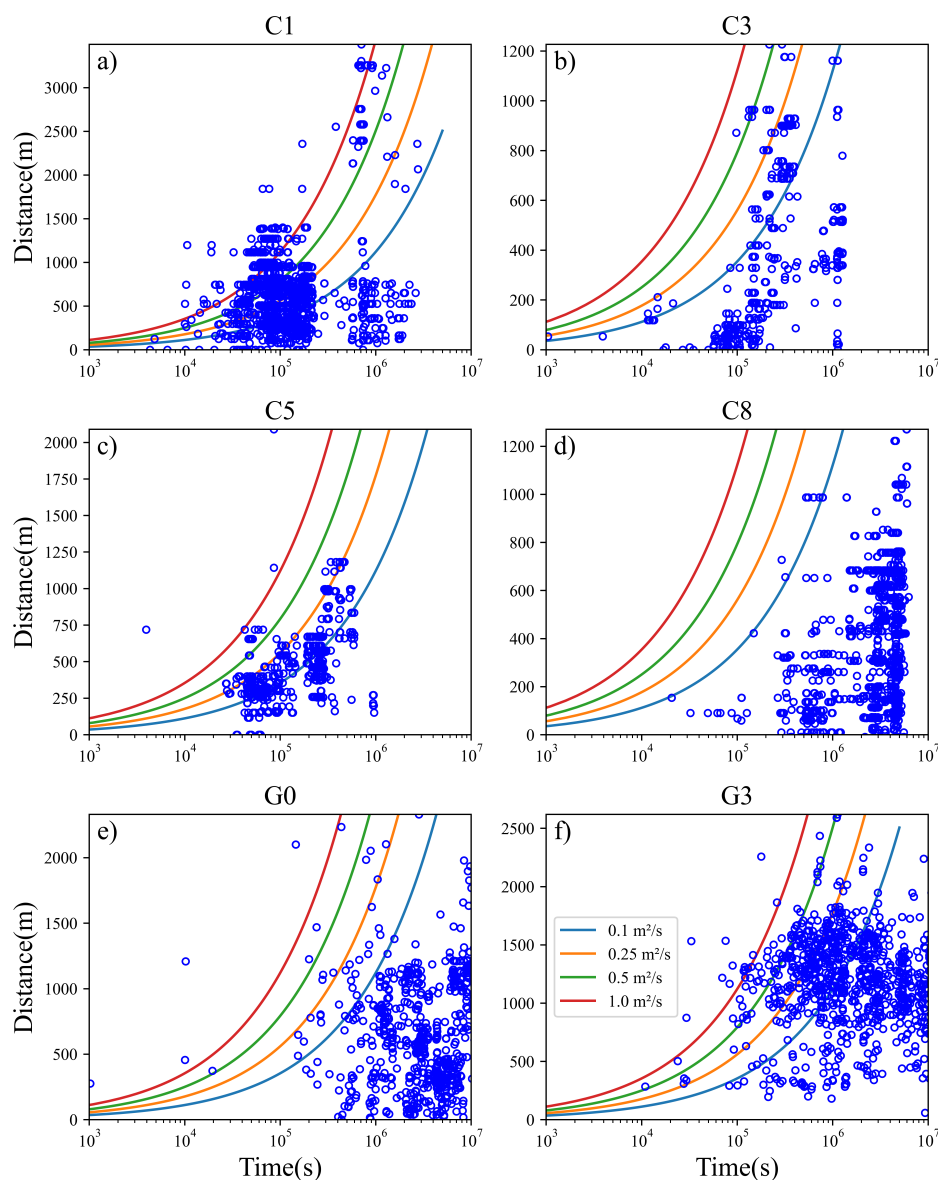
Figure S8   Diffusivity estimates for low-event-count seismic clusters This figure presents diffusivity values (D) for selected clusters characterized by a relatively small number of events, as listed in Table 1. The calculated diffusivity is generally below 1 m²/s, consistent with slow migration patterns and limited spatial expansion of seismicity within these clusters.

References

Brennan Brunsvik, G., Morra, G., Cambiotti, G., Chiaraluce, L., Di Stefano, R., De Gori, P., and Yuen, D. A. Three-dimensional Paganica fault morphology obtained from hypocenter clustering (L'Aquila 2009 seismic sequence, Central Italy). *Tectonophysics*, 804, October 2021.

Campello, R. J. G. B., Moulavi, D., and Sander, J. Density-based clustering based on hierarchical density estimates. In *Pacific-Asia Conference on Knowledge Discovery and Data Mining . Springer*, pages 160–172. Springer, May 2013.

Campello, R. J. G. B., Moulavi, D., Zimek, A., and Sander, J. Hierarchical density estimates for data clustering, visualization, and outlier detection. *ACM Transactions on Knowledge Discovery from Data (TKDD)*, 10(1):1–51, January 2015.

de Berg, M., Gunawan, A., and Roeloffzen, M. Faster DBScan and HDBScan in Low-Dimensional Euclidean Spaces. *International Symposium on Algorithms and Computation*, December 2017.

Ester, M., Kriegel, H.-P., Sander, J., and Xu, X. A density-based algorithm for discovering clusters in large spatial databases with noise. In *Proceedings of the Second International Conference on Knowledge Discovery and Data Mining*, pages 226–231, August 1996.

Faure Walker, J. P., Boncio, P. B., Roberts, G. P., Benedetti, L., Scotti, O., Visini, F., and Peruzza, L. Fault2SHA Central Apennines database and structuring active fault data for seismic hazard assessment. *Scientific Data*, 8(1):87, March 2021.

Hunt, E. L. and Reffert, S. Improving the open cluster census. *Astronomy and Astrophysics*, 646:A104, February 2021. doi: 10.1051/0004-6361/202039341.

Locchi, M. E., Scognamiglio, L., Tinti, E., and Collettini, C. A large fault partially reactivated during two contiguous seismic sequences in Central Italy: The role of geometrical and frictional heterogeneities. *Tectonophysics*, 877:230284, February 2024.

Ma, B., Yang, C., Li, A., Chi, Y., and Chen, L. A Faster DBSCAN Algorithm Based on Self-Adaptive Determination of Parameters. *Procedia Computer Science*, 221:113–120, 2023.

Malagnini, L., Nielsen, S., Mayeda, K., and Boschi, E. Energy radiation from intermediate- to large-magnitude earthquakes: Implications for dynamic fault weakening. *Journal of Geophysical Research*, 115:B06319, June 2010.

Malagnini, L., Lucente, F. P., De Gori, P., Akinci, A., and Munafo', I. Control of pore fluid pressure diffusion on fault failure mode: Insights from the 2009 L'Aquila seismic sequence. *Journal of Geophysical Research*, 117:B05302, May 2012.

Sugan, M., Campanella, S., Chiaraluce, L., Michele, M., and Vuan, A. The unlocking process leading to the 2016 Central Italy seismic sequence. *Geophysical Research Letters*, 50:e2022GL101838, August 2023.

Valoroso, L., Chiaraluce, L., Piccinini, D., Di Stefano, R., Schaff, D., and Waldhauser, F. Radiography of a normal fault system by 64,000 high-precision earthquake locations: The 2009 L'Aquila (central Italy) case study. *Journal of Geophysical Research: Solid Earth*, 118:1156–1176, April 2013.

Waldhauser, F., Michele, M., Chiaraluce, L., Di Stefano, R., and Schaff, D. P. Fault planes, fault zone structure and detachment fragmentation resolved with high-precision aftershock locations of the 2016–2017 Central Italy sequence. *Geophysical Research Letters*, 48(16), August 2021.